Engineering Fracture Mechanics 131 (2014) 269–281

Contents lists available at ScienceDirect

Engineering Fracture Mechanics

journal homepage: www.elsevier.com/locate/engfracmech

A coupled finite element method for the numerical simulation of hydraulic fracturing with a condensation technique

J.Q. Bao *, E. Fathi, S. Ameri

Department of Petroleum and Natural Gas Engineering, West Virginia University, Morgantown, WV 26506, USA

ARTICLE INFO

Article history:
Received 28 January 2014
Received in revised form 1 August 2014
Accepted 2 August 2014
Available online 10 August 2014

Keywords:
Hydraulic fracturing
Finite element method
Condensation technique
M-integral

ABSTRACT

Computation cost is a key issue for finite element methods to simulate hydraulic fracturing. In this paper a coupled finite element method combined with a condensation technique is proposed to address this issue. Removing the node displacements that have no contribution to fracture widths from the coupled equations, the condensation technique reduces the size of the coupled equations in the proposed method. The numerical method with the condensation technique is verified. Simulations show that the condensation technique can reduce the computation cost effectively, in particular when the fracture propagation regime is viscosity-dominated or the simulation is on the early stage. The effects of the condensation technique on the simulation accuracy, stability, and convergence of the numerical method are discussed. The condensation technique is applicable to other finite element methods that are based on linear elastic fracture mechanics.

1. Introduction

Hydraulic fracturing, on one hand, is a natural process such as the magma-driven dike that can propagate in the earth's crust with its length up to tens of kilometers[1,2], and the growth of fracture along glacier beds driven by water[3]. On the other hand, hydraulic fracturing has been accepted as a technique with a variety of applications. These applications include measurement of in-situ stress [4], underground storage of hazardous materials [5], heat production from geothermal reservoirs [6], and barrier walls to prevent containment from transporting [7]. One of the most important applications of hydraulic fracturing nowadays is to improve the recovery of unconventional hydrocarbon reservoirs [8].

Hydraulic fracturing is a coupled process, and this coupled process behaves in two aspects: (1) the deformation of the solid medium and the fracture width are dependent on the fluid pressure in a global manner, and they have the property of non-locality; (2) the fluid flow within fracture is dependent on the fluid pressure and fracture width, and it has the property of non-linearity. These two fundamental properties lead to tremendous difficulty when investigating hydraulic fracturing. Great efforts have been made for the investigation of hydraulic fracturing since the 1950s.

Harrison et al. [9] proposed the first simplified theoretical model, followed by the innovations of some asymptotic models including the PK model [10], PKN model [11], KGD model [12,13], axis-symmetric penny-shaped model[14], and pseudo-3D models [15,16]. Due to the assumptions in these models, there are some limitations for their application [17]. A variety of semi-analytical solutions have been achieved based on the plain strain model whereby the solutions are dependent on the energy consumption regime. The semi-analytical solutions are classified into toughness-dominated ones [18,19] when

* Corresponding author.
E-mail address: bjq05@mails.tsinghua.edu.cn (J.Q. Bao).

http://dx.doi.org/10.1016/j.engfracmech.2014.08.002
0013-7944/

Nomenclature

A	domain for M-integral
A_{tip}	area of the elements on the fracture tip
$\boldsymbol{B}$	to transfer the net pressure into equivalent node forces
$\boldsymbol{B}'$	sub-matrix extracted from $\boldsymbol{B}$
C_l	leak-off coefficient
$\boldsymbol{D}$	elastic stiffness tensor
e_l, e_w	relative errors of half fracture length and fracture width
E	elastic modulus
F	kernel function
$\boldsymbol{F}$	equivalent global nodal force of net pressure
g	leak-off rate
G	shear modulus
$\boldsymbol{H}$	to conclude the contributions of fluid leak-off and fluid injection
K_I	mode-I stress intensity factor
K_{IC}	fracture toughness
$\boldsymbol{K}_{\mathbf{u}}$	global stiffness of the solid elements
$\boldsymbol{K}_{\boldsymbol{w}}$	global flux stiffness of fluid elements
$\boldsymbol{K}_{oo}$, $\boldsymbol{K}_{of}$, $\boldsymbol{K}_{fo}$, $\boldsymbol{K}_{ff}$	sub-matrices extracted from $\boldsymbol{K}_u$
K_m	dimensionless fracture toughness
l_t	half fracture length at moment t
l_n, l_s	half fracture lengths obtained by the numerical method and semi-analytical solutions
$\boldsymbol{L}$	global length stiffness of fluid elements
$\boldsymbol{L}'$	to determine the contribution of node displacements on fracture surface to fracture width
$\boldsymbol{n}$	unit outward normal of fracture
p	net fluid pressure
p_f	fluid pressure
$\boldsymbol{P}$, $\boldsymbol{P}_{n+1}$	node net pressure and node net pressure at the $n+1$-*th* step
$\boldsymbol{q}$	fluid flux
Q_0	injection rate
r_c	characteristic radius
S	collection of boundary conditions of flow
S_e	set of element edges on the fracture
Δt	time step
t	time
t_e	simulation time when l_t equals 14.4 m
t_0	tip arrival time
$\boldsymbol{u}$	displacement
u_x, u_y	displacements in x direction and y direction
u_i, u_i^c	local displacement and auxiliary local displacement
$\boldsymbol{U}$, $\boldsymbol{U}_i (i = n, n+1)$	global nodal displacement and global nodal displacement at the *i-th* step
$\boldsymbol{U}^o_{n+1}$	node displacement without contribution to fracture width at the $n+1$-*th* step
$\boldsymbol{U}^f_i (i = n,\ n+1)$	node displacement with contribution to fracture width at the *i-th* step
w	fracture width
$\boldsymbol{W}$	a vector formed by the widths on of the nodes on fracture surface
$\boldsymbol{W}_i (i = n, n+1)$	fracture width at the *i-th* step
$\boldsymbol{W}^{(i)} (i=0, m, m+1)$	fracture width at the *i_th* iteration
$x_j (j=1, 2)$	local coordinate

Greek letters

δp	allowable testing function
δ_t	dimensionless simulation time
δ_{ij}	Kronecker delta
$\boldsymbol{\varepsilon}$, ε_{mn}	strain
ε^s_{tol}, ε^w_{tol}	tolerance for stress intensity factor and fracture width
ν	Poisson's ratio
ξ	dimensionless x coordinate
ρ	local radial coordinate
$\boldsymbol{\sigma}$, σ_{ij}	stress

σ_0	confining stress
σ_{ij}^c	auxiliary stress
θ	local angular coordinate
μ	fluid dynamic viscosity
χ	scalar field

the energy is mainly consumed by the fracture propagation, the viscosity-dominated ones when the energy is mainly consumed by the flow of the viscous fluid within the fracture [20–22], and the intermediate regime for other situations [23]. These semi-analytical solutions can be served as benchmarks for numerical models [22].

The conventional method for the numerical simulation of hydraulic fracturing are the discontinuous displacement (DD) methods [24–31], which are based on linear elastic fracture mechanics (LEFM) and a variant of the boundary element method [32]. There exists great difficulty for the DD methods to find their non-local kernel functions when the model has a complex structure, for example if the model is multi-layered [28]. Finite element methods have greater flexibilities than the DD methods for the numerical simulation of hydraulic fracturing, because they do not depends on the kernel functions. A variety of finite element methods have been proposed to simulate hydraulic fracturing. Chen et al. [33] and Chen [34] used a finite element method and investigated hydraulic fracturing in impermeable mediums. Carrier and Granet [35] discussed the effects of permeability on fracture propagation, and Papanastasiou [36] investigated the effect of rock plasticity. Hunsweck et al. [37] proposed a coupled finite element method to simulate hydraulic fracturing with fluid lag. Fu et al. [38] discussed the interaction between hydraulic fractures and natural fractures.

There are two key issues for finite element methods to simulate hydraulic fracturing. The firs issue is model remeshing as fractures continually propagate. The second issue is high computation cost [37,38]. A variety of measurements have been used to address the first issue. These measurements includes the predefinition of the fracture propagation path [33–36], the application of node-split technique [38], and the introduction of the extended finite element methods [39–43].

In this paper we are focused on addressing the second issue. One reason for the high computation cost in the finite element methods is that the sizes of their equations are large, as they always depend on the number of the nodes in the whole model. In this paper we introduced a coupled LEFM-based finite element method and a condensation technique. The condensation technique removes the node displacements that have no contribution to fracture width from the coupled equations. It reduces the size of the coupled equations greatly and results in the decrease of computation cost. This condensation technique is independent of model remeshing techniques, and it is applicable to other finite element simulators that take LEFM as their theoretical foundation.

Some assumptions are made in this paper for simplicity. These assumptions include uniform confining stress, zero gaps between the fluid front within the fracture and the fracture tip, and a straight fracture propagation path that is perpendicular to the confining stress. The rest of this paper is organized as follows: the theoretical model of hydraulic fracturing in plane strain is presented in Section 2. The finite element method and the condensation technique are introduced in Section 3. Some numerical aspects of the method are presented in Section 4. The method with the condensation technique is verified and the impacts of the condensation technique on the numerical method are discussed in detail in Section 5. Conclusions are made in Section 6.

2. Theoretical model

As shown in Fig. 1(a), the momentum of fracture propagation in hydraulic fracturing is from the injection of incompressible Newtonian fluid with rate Q_0. The bi-wing fracture propagates perpendicular to the direction of far-field least principle

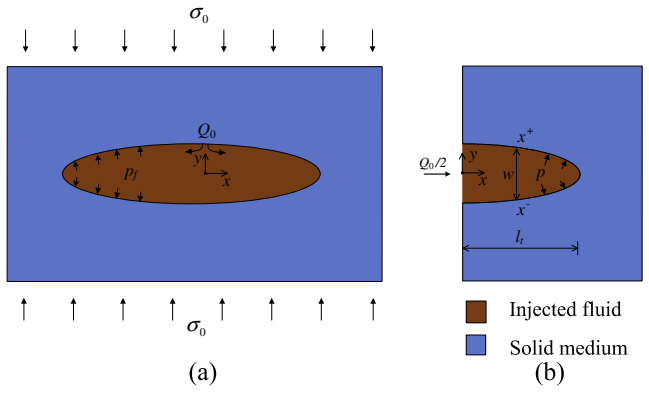

Fig. 1. Sketch of a plane-strain fluid-driven fracture (a) and its equivalent model (b).

stress σ_0 as shown in Fig. 1(a). σ_0 is referred to as confining stress and is positive when compressive. The injection point is the center of the bi-wing fracture, and it is also the origin of the Cartesian coordinates used in this paper. The fracture width w results from the action of the confining stress σ_0 and the fluid pressure p_f. As the confining stress is uniform, the homogeneous model in Fig. 1(a) can be represented by its half model as shown in Fig. 1(b). Net pressure is defined as the fluid pressure minus the confining stress, and it is denoted as p. In the equivalent model only net pressure p contributes to the fracture width [17]. The theoretical model has two parts, which are the elastic response of the solid medium and the fluid flow within the fracture.

2.1. Elastic response of the solid medium

The elastic response at any point $\boldsymbol{x}$ in Fig. 1(b) is governed by the equivalence condition and the constitutive law, of which the equations are

$$\nabla \cdot \boldsymbol{\sigma} = 0 \tag{1}$$

and

$$\boldsymbol{\sigma}(\boldsymbol{x}) = \boldsymbol{D} : \boldsymbol{\varepsilon}(\boldsymbol{x}) \tag{2}$$

In Eq. (1), $\boldsymbol{\sigma}$ is the stress tensor and $(\nabla\cdot)$ is the divergence operator. In Eq. (2), $\boldsymbol{D}$ is the elastic stiffness tensor of the solid media, $(:)$ is the double dot product operator between two tensors, and $\boldsymbol{\varepsilon}$ is the strain tensor and equals the symmetric part of the gradient of displacement $\boldsymbol{u}$, i.e.,

$$\boldsymbol{\varepsilon} = [\nabla \boldsymbol{u} + (\nabla \boldsymbol{u})^T]/2 \tag{3}$$

In Eq. (3), (∇) is the gradient operator, and superscript T indicates transpose.

The stress boundary condition can be expressed as

$$\boldsymbol{\sigma}(x, 0) \cdot \boldsymbol{n} = -p(x, t) \quad x \leqslant l_t \tag{4}$$

where $\boldsymbol{n}$ is the unit outward normal of the fracture, l_t as shown in Fig. 1(b) is the half fracture length at moment t. The displacement boundary condition in Fig. 1(b) is expressed as

$$u_x(0, y) = 0 \tag{5}$$

where u_x is the displacement in x direction.

It is seen in Fig. 1(b) that at any moment t, we have

$$w(x) = [u_y(\boldsymbol{x}^+) - u_y(\boldsymbol{x}^-)] \tag{6}$$

where $w(x)$ is the fracture width at point $(x, 0)$, u_y is the displacement in y direction, and $\boldsymbol{x}^+$ and $\boldsymbol{x}^-$ are two points on the fracture surface as shown in Fig. 1(b). These two points are actually the same point $\boldsymbol{x}(x, 0)$ before fracture tip reaches there.

In hydraulic fracturing fracture propagation is mode-I dominated, and the propagation criterion is

$$K_I = K_{IC} \tag{7}$$

where K_I is the mode-I stress intensity factor (SIF), and K_{IC} is the fracture toughness of the solid medium.

2.2. Fluid flow within the fracture

The one-dimensional fluid flow within the fracture is modeled with lubrication theory, and its governing equation is described by Poiseuille's law [44], i.e.,

$$\boldsymbol{q} = -\frac{w^3}{12\mu}\nabla p_f \tag{8}$$

where $\boldsymbol{q}$ is the fluid flux, μ is the fluid viscosity, and (∇) is the gradient operator defined in x direction. It is seen in Eq. (8) that the fluid flow is non-linearly dependent on the fracture width. For the case of uniform confining stress and zero fluid lag, p_f in Eq. (8) can be replaced by p. Therefore, we have

$$\boldsymbol{q} = -\frac{w^3}{12\mu}\nabla p \tag{9}$$

Just like some semi-analytical solutions [19,22,23], Carter's model [45] is used to simulate leak-off in the proposed method. The leak-off model is cast as

$$g(x, t) = \frac{2C_l}{\sqrt{t - t_0(x)}} \tag{10}$$

where C_l is leak-off coefficient, and t_0 is the fracture tip arrival time.

The conservation of the incompressible fluid in the fracture leads to [46]

$$\frac{\partial w}{\partial t} + \nabla \cdot \boldsymbol{q} + g = 0 \tag{11}$$

where $(\nabla\cdot)$ is the divergence operator defined in x direction. The boundary conditions for fluid flow in the fracture are

$$\boldsymbol{q}(x = 0^+, t) = Q_0/2, \quad \boldsymbol{q}(x = l_t, t) = 0 \tag{12}$$

The zero flux at the fracture tip in Eq. (12) originates from zero fracture width at the tip [22], which can be seen in Eq. (9).

3. Numerical method

3.1. Finite element analysis

Discretizing the equivalent model with finite elements as shown in Fig. 2, we can achieve a finite element equation for the solid medium according to Eqs. (1)–(5) as

$$\boldsymbol{K}_u \boldsymbol{U} = \boldsymbol{F} \tag{13}$$

where $\boldsymbol{K}_u$ is the global stiffness of the solid elements, $\boldsymbol{U}$ is the global nodal displacement, and $\boldsymbol{F}$ is the equivalent global nodal force of the net pressure.

As only net pressure has contribution to $\boldsymbol{F}$, Eq. (13) can be rewritten as

$$\boldsymbol{K}_u \boldsymbol{U} - \boldsymbol{B}\boldsymbol{P} = \boldsymbol{0} \tag{14}$$

where $\boldsymbol{P}$ is a vector formed by the node net pressure, and matrix $\boldsymbol{B}$ transfers the net pressure into equivalent node forces.

Eq. (11) leads to its weak form [25] as

$$\int_{l_t} \left[-\nabla(\delta p) \cdot \boldsymbol{q} + (\delta p)\frac{\partial w}{\partial t} + (\delta p) g \right] dl + \delta p q|_S = 0 \tag{15}$$

where δp is any allowable testing function, and S is the collection of boundary conditions of flow. Therefore, a finite element equation for fluid flow within the fracture is cast as

$$\boldsymbol{K}_w(\boldsymbol{W})P + L\dot{\boldsymbol{W}} + \boldsymbol{H} = \boldsymbol{0} \tag{16}$$

where $\boldsymbol{W}$ is a vector formed by the widths of the nodes on the fracture surface, $\boldsymbol{K_w}$ is the assembly of the flux stiffness of the fluid elements and it is a function of $\boldsymbol{W}$, $\boldsymbol{L}$ is the assembly of the length stiffness of the fluid elements, and $\boldsymbol{H}$ concludes the contributions of the fluid leak-off and the fluid injection.

Taking time integration with Eq. (16), we have

$$\int_{t_n}^{t_{n+1}} [\boldsymbol{K}_w(\boldsymbol{W})\boldsymbol{P} + \mathbf{L}\dot{\boldsymbol{W}} + \boldsymbol{H}] dt = \boldsymbol{0} \tag{17}$$

Backward Euler scheme for time difference is used in this paper. So according to Eq. (17) we have

$$\boldsymbol{K}_w(\boldsymbol{W}_{n+1})\boldsymbol{P}_{n+1}\Delta t - \mathbf{L}(\boldsymbol{W}_{n+1} - \boldsymbol{W}_n) + \boldsymbol{H}\Delta t = \boldsymbol{0} \tag{18}$$

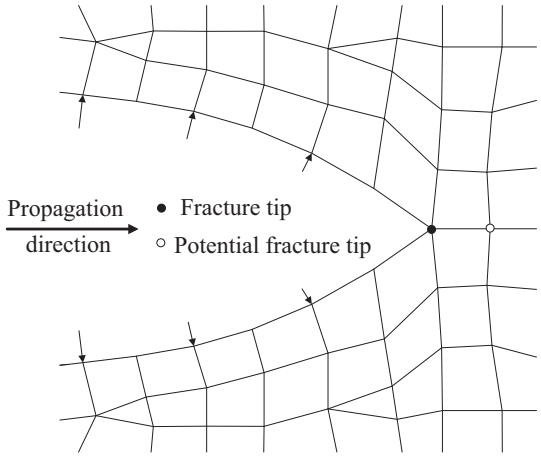

Fig. 2. Discretization of the solid medium with finite elements.

where $\boldsymbol{W}_{n+1}$ and $\boldsymbol{P}_{n+1}$ are the unknown fracture width and net fluid pressure at the $n+1$-*th* step, respectively, $\boldsymbol{W}_n$ is the known fracture width at the *n-th* step, and Δt is the time step between the *n-th* step and the $n+1$-*th* step.

According to Eq. (6), Eq. (18) can be rewritten in an alternative way as

$$\boldsymbol{K}_w(\boldsymbol{U}_{n+1})\boldsymbol{P}_{n+1}\Delta t + \boldsymbol{L}'\left(\boldsymbol{U}^f_{n+1} - \boldsymbol{U}^f_n\right) + \boldsymbol{H}\Delta t = \boldsymbol{0} \tag{19}$$

where $\boldsymbol{U}^f_{n+1}$ and $\boldsymbol{U}^f_n$ are the displacements of the nodes on the fracture surface at the $n+1$-*th* step and *n-th* step, respectively, and $\boldsymbol{L}'$ determines the contribution of node displacements on the fracture surface to fracture widths. Note that $\boldsymbol{U}^f_{n+1}$ is a subset of $\boldsymbol{U}_{n+1}$, and $\boldsymbol{U}^f_n$ is known a priori.

In every step, Eq. (18) leads to a new equation written as

$$\boldsymbol{K}_u\boldsymbol{U}_{n+1} - \boldsymbol{B}\boldsymbol{P}_{n+1} = \boldsymbol{0} \tag{20}$$

$\boldsymbol{U}_{n+1}$ and $\boldsymbol{P}_{n+1}$ can be obtained by solving the coupled Eqs. (19) and (20).

3.2. Condensation technique

A coupled scheme [17] is used in this paper, which means that the coupled Eqs. (19) and (20) are solved together. It is seen that the number of unknowns of Eq. (19) is dependent on the nodes on the fracture surface. However, the number of unknowns of Eq. (21) is dependent on the nodes in the whole model. A condensation technique [47] is introduced to reduce the unknowns in the coupled equations.

Let $\boldsymbol{U}^o_{n+1}$ denote the node displacements at the $n+1$-*th* step that have no contribution to fracture widths. Note that there is no equivalent node force for nodes outside the fracture surface. Eq. (20) can be reorder and rewritten as

$$\begin{bmatrix} \boldsymbol{K}_{oo} & \boldsymbol{K}_{of} & \boldsymbol{0} \\ \boldsymbol{K}_{fo} & \boldsymbol{K}_{ff} & -\boldsymbol{B}' \end{bmatrix} \begin{Bmatrix} \boldsymbol{U}^o_{n+1} \\ \boldsymbol{U}^f_{n+1} \\ \boldsymbol{P}_{n+1} \end{Bmatrix} = \boldsymbol{0} \tag{21}$$

where sub-matrices $\boldsymbol{K}_{of}$, $\boldsymbol{K}_{oo}$, $\boldsymbol{K}_{fo}$, and $\boldsymbol{K}_{ff}$ are extracted from $\boldsymbol{K}_u$, and sub-matrix $\boldsymbol{B}'$ is extracted from $\boldsymbol{B}$. Eq. (21) is decomposed into a condensation equation

$$\left(\boldsymbol{K}_{ff} - \boldsymbol{K}_{fo}\boldsymbol{K}^{-1}_{oo}\boldsymbol{K}_{of}\right)\boldsymbol{U}^f_{n+1} - \boldsymbol{B}'\boldsymbol{P}_{n+1} = \boldsymbol{0} \tag{22}$$

and a $\boldsymbol{P}$-free equation

$$\boldsymbol{K}_{of}\boldsymbol{U}^f_{n+1} + \boldsymbol{K}_{oo}\boldsymbol{U}^o_{n+1} = \boldsymbol{0} \tag{23}$$

With the condensation technique, Eqs. (19) and (22) rather than Eqs. (19) and (20) can be solved at first in every step. The Newton–Raphson algorithm [48] is used to solve these coupled non-linear equations. It is seen that the number of unknowns in the coupled Eqs. (22) and (23) is only determined by the nodes on the fracture surface. With the removal of the displacements that have no contribution to fracture widths from the coupled equations by the condensation technique, the proposed method avoids solving large-scaled equations during the Newton–Raphson iterations in every step.

The prerequisite of the condensation technique is that $\boldsymbol{K}_{of}$ and $\boldsymbol{K}_{oo}$ are independent of $\boldsymbol{U}$. The condensation technique is used whenever fractures propagate. Therefore, the condensation technique is applicable to other finite element methods that are based on LEFM regardless of their measurements for model remeshing.

4. Some numerical aspects

A key aspect for the finite element method is the calculation of SIF. The M-integral method [49] is used in this paper to calculate SIF. In the M-integral method, the approximation of K_I in the plane strain model is

$$K_I = \frac{2E}{1-\nu}\left\{\int_A \left[\sigma_{ij}\frac{\partial u^c_i}{\partial x_1} + \sigma^c_{ij}\frac{\partial u_i}{\partial x_1} - \sigma^c_{mn}\varepsilon_{mn}\delta_{1j}\right]\frac{\partial \chi}{\partial x_j}dS - \int_{S_e}\chi p\frac{\partial u^c_i}{\partial x_1}dL\right\} \tag{24}$$

where E is the elastic modulus, v is the Poisson's ratio, domain A as shown in Fig. 3 is a set of elements around the fracture tip, S_e is a set of edges of the finite elements in set A and these edges coincide with the fracture surface shown in Fig. 3 with dashed line, σ_{ij} is the stress, u_i is the local displacement, x_j is the local coordinate, δ_{ij} is the Kronecker delta, χ is a scalar field, ε_{mn} is the strain, and σ^c_{ij} and u^c_i are the auxiliary stress and displacement, respectively. Einstein summation convention is used for repeated indices in Eq. (24).

The characteristic radius r_c of the fracture tip is defined for the determination of domain A, and

$$r_c = \sqrt{A_{tip}} \tag{25}$$

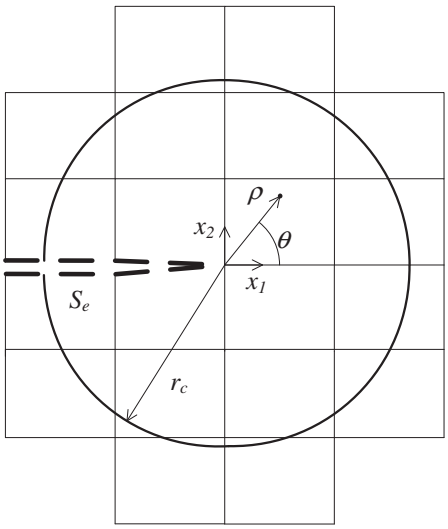

Fig. 3. Domain for the interaction integral.

where A_{tip} is the summation of the area of the elements which share the node on the fracture tip. Elements having node(s) in the circle as shown in Fig. 3 set up the domain A, and the radius of the circle equals r_c. The scalar χ is taken to have a value of unity for nodes in the circle, and zero for nodes out of the circle [37].

The analytical solutions of the auxiliary displacement u_i^c are [50]

$$\begin{aligned} u_1^c &= \frac{1}{2G}\sqrt{\frac{\rho}{2\pi}}\left\{\cos\frac{\theta}{2}[(3-4\nu)-\cos\theta]\right\} \\ u_2^c &= \frac{1}{2G}\sqrt{\frac{\rho}{2\pi}}\left\{\sin\frac{\theta}{2}[(3-4\nu)-\cos\theta]\right\} \end{aligned} \tag{26}$$

where G is the shear modulus, ν is the Poisson's ration of the solid medium, and ρ and θ are the polar coordinates as shown in Fig. 3. The auxiliary stress can be calculated based on Eq. (26) and the elastic constitutive law.

A node-split technique [38] is used to remesh the model when fracture propagates. In the node-split method, the node at the fracture tip as shown in Fig. 2 is split into two nodes when fracture propagates. If the fracture propagates along a straight line, the node right ahead of the fracture tip becomes the new fracture tip when fracture propagates, and it is defined as the potential fracture tip and shown in Fig. 2.

The convergence criterion for the Newton–Raphson iterations is

$$e_w = \|\boldsymbol{W}^{(m)} - \boldsymbol{W}^{(m-1)}\| / \|\boldsymbol{W}^{(m)} - \boldsymbol{W}^{(0)}\| \leqslant \varepsilon_{tol}^w \tag{27}$$

where e_w is defined as the relative error of fracture width, $\|\|$ is the 2-norm operator, $\boldsymbol{W}^{(i)}$ ($i = 0$, $m-1$, and m) is the fracture width at the *i_th* iteration and superscript 0 indicates initial guess, and ε_{tol}^w is the specified tolerance for fracture widths and it equals 1.0e−8 in this paper.

Dynamic time step Δt is used to ensure that in every step we have

$$K_{IC} \leqslant K_I \leqslant (1.0 + \varepsilon_{tol}^s) K_{IC}, \tag{28}$$

where ε_{tol}^s is the allowable tolerance for SIF, which is taken as 0.001 in this paper.

5. Verification and discussion

5.1. Verification

The coupled method can be verified by comparing its results with some semi-analytical solutions. The semi-analytical solutions are dependent on dimensionless toughness K_m, which is defined as [23]

$$K_m = 4\left(\frac{2}{\pi}\right)^{1/2} \frac{K_{IC}(1-\nu^2)}{E}\left[\frac{E}{12\mu Q_0(1-\nu^2)}\right]^{1/4} \tag{29}$$

The hydraulic fracturing propagation regime is toughness-dominated when K_m is larger than 4.0, and it is viscosity-dominated when K_m is smaller than 1.0 [23].

Table 1
Material properties and operation parameters in the model.

Elastic modulus	E	18000 MPa
Poisson' s ratio	υ	0.2
Fracture toughness	K_{IC}	4.00 MPa $m^{0.5}$ (large toughness, $K_m = 4.53$)
		0.20 MPa $m^{0.5}$ (large viscosity, $K_m = 0.28$)
Leak-off coefficient	C_l	7.0e−5 m $s^{1/2}$ (large toughness)
		0.0 m $s^{1/2}$ (large viscosity)
Dynamic viscosity	μ	7.98e−7 KPa s
Injection rate	Q_0	0.001 m^2_fs

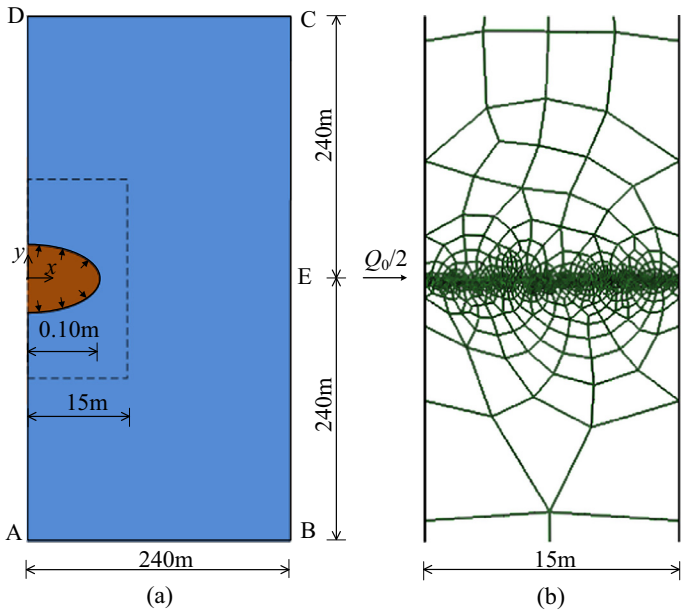

Fig. 4. The rectangle model (not scaled) (a) and its elements around the fracture propagation path.

There are two examples in the verification, one for the toughness-dominated regime with leak-off and the other for the viscosity-dominated regime without leak-off. The semi-analytical solutions are investigated by Bunger et al. [19] for the toughness-dominated regime with leak-off, and by Adachi and Detournay [21] for the viscosity-dominated regime without leak-off. The simulations were run on an in-house program coded with Fortran 90.

The material properties and operation parameters for the two examples are listed in Table 1.

The rectangle model for the two examples is shown in Fig. 4(a), where the initial horizontal fracture lies in the middle of the left edge. In all the simulations, the maximum half fracture length is expected to be smaller than 15.0 m. Let l_e denote the characteristic size of the elements on the fracture propagation path. It equals 0.06 m in the model. The elements around the fracture propagation path are shown in Fig. 4(b). There are 4330 linear quad elements and 4437 nodes in the initial model. The initial half fracture length equals 0.06 m, and its initial uniform net pressure equals 0.05 MPa. Edge AD is fixed in x direction, point E is fixed in y direction.

The dimensionless simulation time δ_t is defined as

$$\delta_t = t/t_e \tag{30}$$

where t_e means the simulation time when l_t reaches 14.4 m in the numerical solutions, and it equals 104.65 and 16.31 s in the two examples, respectively. Similarly, a dimensionless x coordinate ξ can be defined. ξ equals 0 at the injection point, and equals 1 at the fracture tip. Some results of the numerical method with the condensation technique and the semi-analytical solutions are shown in Fig. 5. The results include the net pressure at the injection point, the fracture width at the injection point, the evolutions of half fracture length, and a net pressure profile.

The numerical method and the semi-analytical solutions share the same theoretical basis. It is seen in Fig. 5 that there are small gaps between the numerical results and the semi-analytical solutions. There are two fundamental reasons for these gaps. Firstly, the semi-analytical solutions correspond to limit situations. In the tough-dominated semi-analytical solution, it is assumed that the fluid viscosity is zero, and the net fluid pressure is uniform. In the viscosity-dominated semi-analytical

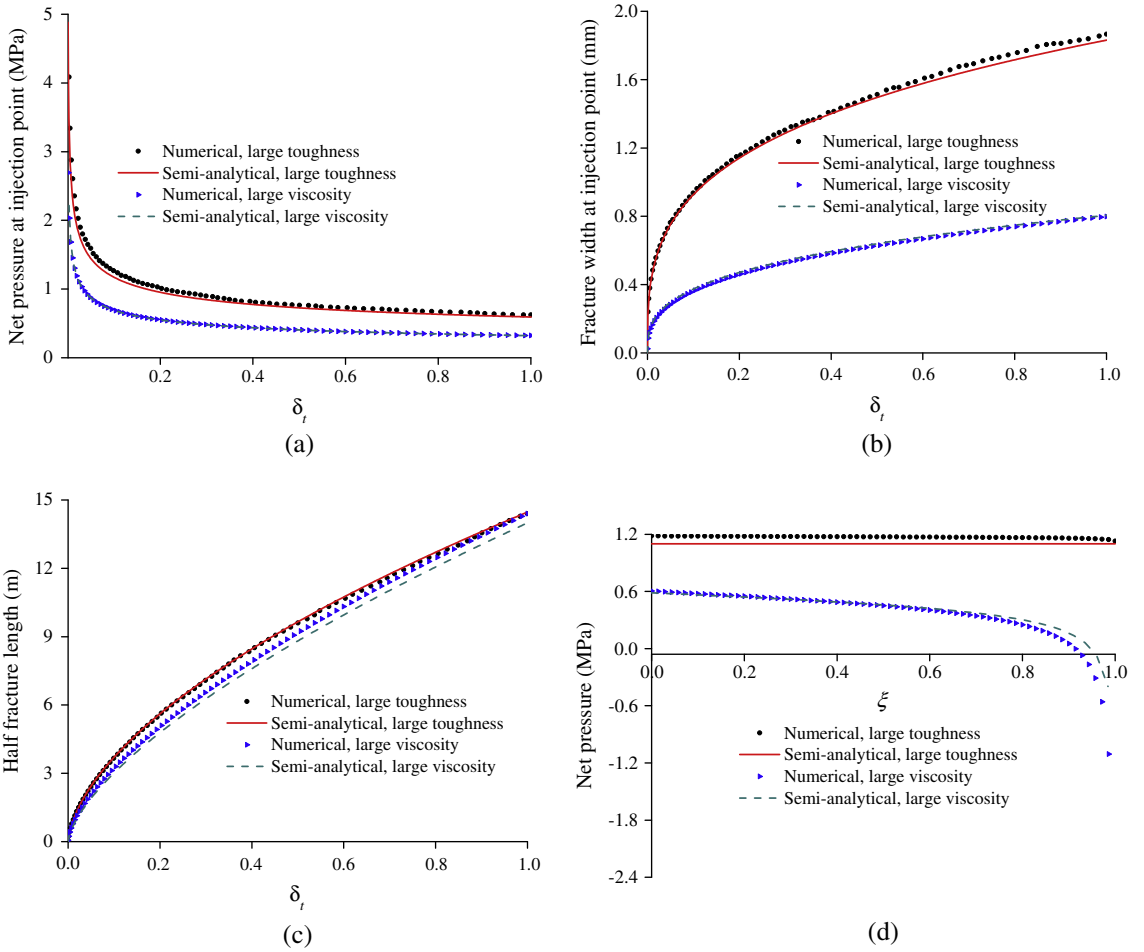

Fig. 5. Numerical results and semi-analytical solutions of net pressure at injection point (a), fracture width at injection point (b), half fracture length (c), and net pressure profile (l_t = 4.2 m) (d).

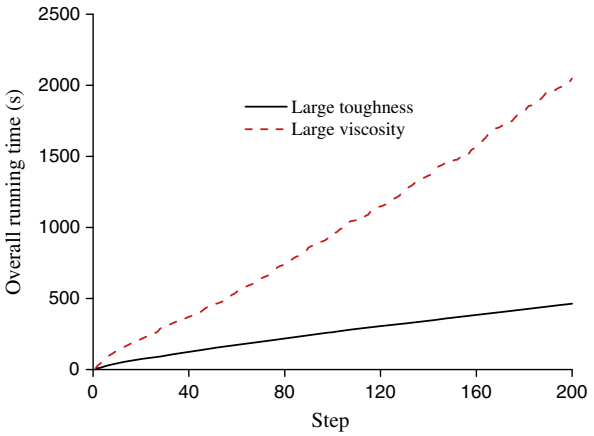

Fig. 6. Overall program running time when the condensation technique is not used and l_e equals 0.04 m.

solution, it is assumed that the fracture toughness is zero, and the net pressure at the fracture is negative and infinite. Secondly, the models in the semi-analytical solutions are infinite, and the models in the numerical examples are finite. The numerical results have good agreements with the semi-analytical solutions. This means that the numerical method with

the condensation technique is verified. Both the numerical results and the semi-analytical solutions in Fig. 5(d) show that the fracture tip behavior in the large viscosity example is more singular than that in the large toughness one.

5.2. Effects of the condensation technique

To discuss the effect of the condensation technique, two additional meshes are used to discretize the rectangle model of the two examples in the verification sub-section, where l_e equals 0.04 m and 0.08 m, respectively. For the mesh with l_e equal to 0.04 m, the initial model has 4650 quad elements and 4656 nodes, and for the mesh with l_e equal to 0.08 m, the initial model has 4081 elements and 4192 nodes. The initial half fracture lengths in the two meshes are 0.04 m and 0.08 m, respectively. Their initial net pressure is also 0.05 MPa. The two examples with the new meshes are simulated by the numerical method with and without the condensation technique. For the simulations where the condensation technique is not used and l_e equal 0.04 m, the overall program running time after each of the first 200 steps is shown in Fig. 6. It is seen in Fig. 6 that much more computation cost is needed in the large viscosity example than that in the large toughness one. Similar phenomena are also observed when l_e equals 0.06 m and 0.08 m.

The acceleration index is defined as the ratio of overall program running time for the simulations with the condensation technique over that without the condensation technique. The evolutions of the acceleration index over the simulation time in the two examples are plotted in Fig. 7. It is seen in Fig. 7 that the computation cost is reduced greatly if the condensation technique is used. The condensation technique exceedingly accelerates the simulations when the simulation is on its early stage. Although the acceleration indices decrease when fracture propagates, they gradually get stable and are far greater than 1.0. It is also seen in Fig. 7 that the condensation technique plays a more effective role in the large viscosity example than in the large toughness example when the same mesh is used.

The relative error of half fracture length, i.e., e_l, is defined as

$$e_l = |l_n - l_s|/l_s \tag{31}$$

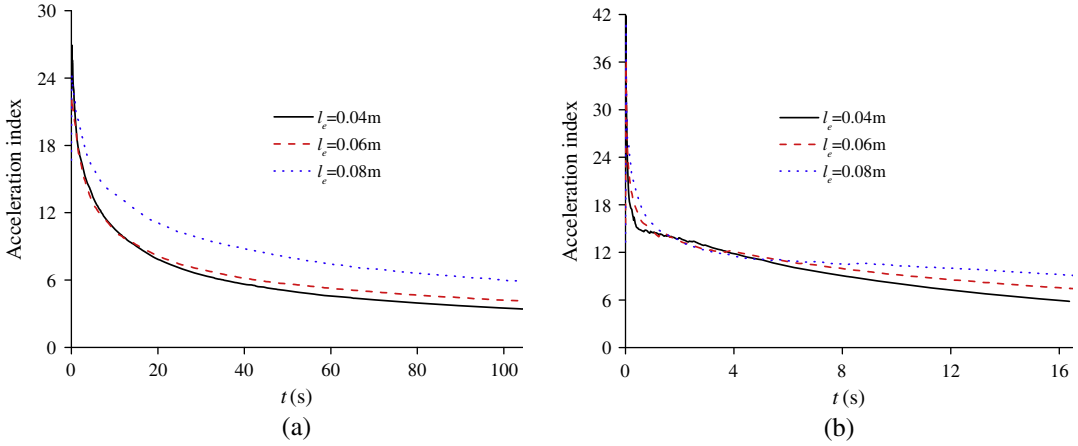

Fig. 7. Evolutions of α s in the two examples: (a) large toughness; (b) large viscosity.

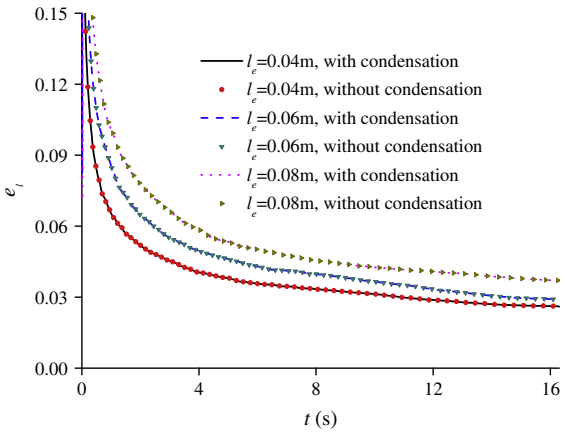

Fig. 8. e_l s in the large toughness example.

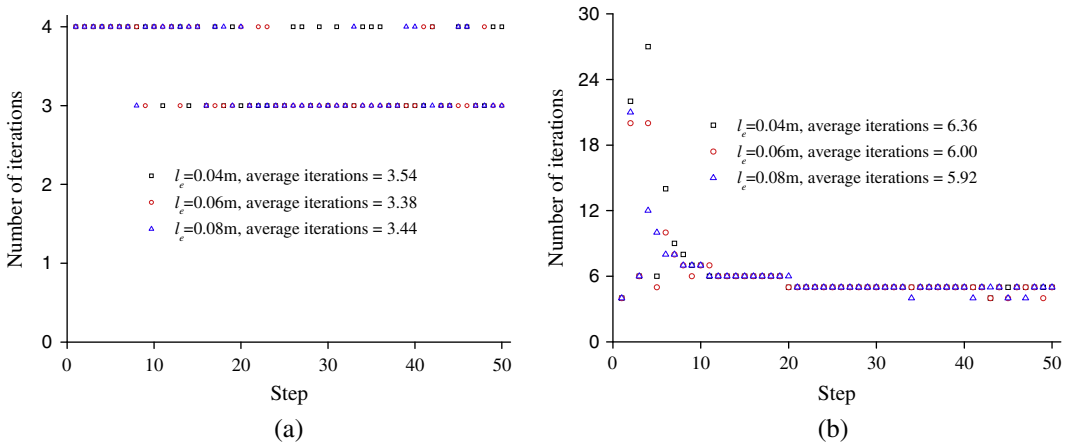

Fig. 9. Number of iteration for the first 50 steps in the two examples: (a) large toughness example; (b) large viscosity example.

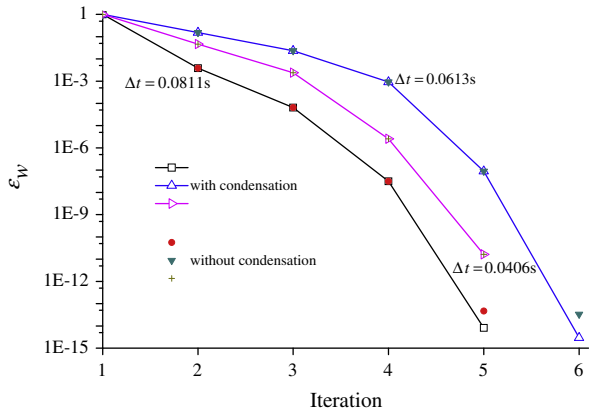

Fig. 10. Convergence tendencies in trial time steps.

where l_n and l_s are half fracture lengths obtained by the numerical method and semi-analytical solutions at the same time, respectively. e_l s in the large viscosity example are shown in Fig. 8. It is seen in Fig. 8 that for the same l_e and the simulation time, the related errors induced by the method with the condensation technique are almost identical to those without the condensation technique. The errors induced by the condensation technique are ignorable for the large viscosity example. Similar situations are also found in the large toughness example.

The numbers of iterations needed to solve the non-linear coupled equations in the two examples are plotted in Fig. 9 for their first 50 steps when the condensation technique is used. It is seen in Fig. 9 in most steps the solutions get convergent within 6 steps regardless of the fracture propagation regime. It is also seen in Fig. 9 that the average number of iterations is not sensitive to the mesh size. We found that the condensation technique has very limited effect on the number of iterations in all the simulations. For example when the condensation technique is used and l_e equals 0.06 m, the average number of iterations for the first 50 steps in the large toughness example equals 3.38, which is close to 3.34 when the condensation technique is not used. This means the condensation technique does not deteriorate the structure of the coupled equations. More iteration effort is needed on average in the large viscosity example than in the large toughness example. The reason is that the fracture tip behavior in the large viscosity example is more singular.

Time steps were selected by trial and error to satisfy Eq. (28). No numerical instability occurred in the simulations. The convergence tendencies of ε_w for some trail time steps in the large viscosity example are illustrated in Fig. 10 representatively. These trial time steps have the same initial conditions and their l_e equals 0.08 m. It is seen in Fig. 10 that e_w s drop sharply with iterations for all the trial steps. The numerical method exhibits excellent robustness, and the condensation technique does not worsen its convergence.

6. Conclusion

In this paper a coupled finite element method with a condensation technique is proposed for the simulation of hydraulic fracturing. The condensation technique reduces the size of the coupled equations in the numerical method and lowers the

computation cost. The numerical method with the condensation technique is verified by comparing its numerical results with semi-analytical solutions. Simulations show that the condensation technique has noticeable acceleration effects, especially when the simulations are on the early stages. Although the large viscosity simulations need more computation efforts than the large toughness ones in the proposed method, the condensation technique plays a more effective role for them. The ill effects of the condensation technique on the simulation accuracy, stability, and convergence of the proposed method are marginal and ignorable. The condensation technique can be easily implanted to other finite element simulators that are based on linear elastic fracture mechanics.

Acknowledgements

Funding for this project is provided by RPSEA through the "Ultra-Deepwater and Unconventional Natural Gas and Other Petroleum Resources" program authorized by the U.S. Energy Policy Act of 2005. RPSEA (www.rpsea.org) is a nonprofit corporation whose mission is to provide a stewardship role in ensuring the focused research, development and deployment of safe and environmentally responsible technology that can effectively deliver hydrocarbons from domestic resources to the citizens of the United States. RPSEA, operating as a consortium of premier U.S. energy research universities, industry, and independent research organizations, manages the program under a contract with the U.S. Department of Energy's National Energy Technology Laboratory. The first author would like to thank Prof. Detournay for his invaluable suggestions.

References

[1] Lister JR. Buoyancy-driven fluid fracture: the effects of material toughness and of low-viscosity precursors. J Fluid Mech 1990;210:263–80.
[2] Spence DA, Turcotte DL. Magma-driven propagation of cracks. J Geophys Res 1985;90:575–80.
[3] Tsai VC, Rice JR. A model for turbulent hydraulic fracture and application to crack propagation at glacier beds. J Geophys Res 2010;115:1–18.
[4] Hayashi K, Haimson BC. Characteristics of shut-in curves in hydraulic fracturing stress measurements and determination of in situ minimum compressive stress. J Geophys Res 1991;96(B11):18311–21.
[5] Levasseur S et al. Hydro-mechanical modelling of the excavation damaged zone around an underground excavation at Mont Terri Rock Laboratory. Int J Rock Mech Min Sci 2010;47(3):414–25.
[6] Legarth B, Huenges E, Zimmermann G. Hydraulic fracturing in sedimentary geothermal reservoir: results and implications. Int J Rock Mech Min Sci 2005;42(7–8):1028–41.
[7] Murdoch LC. Mechanical analysis of idealized shallow hydraulic fracture. J Geotechn Geoenviron Engng 2002;128(6):289–313.
[8] Bunger AP. Analysis of the power input needed to propagate multiple hydraulic fracture. Int J Solids Struct 2013;50:1538–49.
[9] Harrison E, Kieschnick WF, McGuire WJ. The mechanics of fracture induction and extension. Petrol Trans AIME 1954;201:252–63.
[10] Perkins T, Kern L. Widths of hydraulic fractures. J Petrol Technol 1961;13(9):937–49.
[11] Nordren RP. Propagation of a vertical hydraulic fracture. SPE 7834 1972;12(8):306–14.
[12] Geertsma J, De Klerk F. A rapid method of predicting width and extent of hydraulically induced fractures. J Petrol Technol 1969;21(12):1571–81.
[13] Khristianovic SA, Zheltov YP. Formation of vertical fractures by means of highly viscous liquid. In: Proceedings of the fourth world petroleum congress. Rome; 1955.
[14] Abe H, Mura T, Keer L. Growth-rate of a penny-shaped crack in hydraulic fracturing of rocks. J Geophys Res 1976;81(29):5335–40.
[15] Advani SH, Lee TS, Lee JK. Three-dimensional modeling of hydraulic fractures in layered media: part I—finite element formulations. J Energy Res Technol 1990;112(1):1–9.
[16] Vandamme L, Curran JH. A three-dimensional hydraulic fracturing simulator. Int J Numer Meth Engng 1989;28:909–27.
[17] Adachi J et al. Computer simulation of hydraulic fractures. Int J Rock Mech Min Sci 2007;44(5):739–57.
[18] Garagash DI. Plain-strain propagation of a fluid-driven fracture during injection and shut-in: asymptotics of large toughness. Engng Fract Mech 2006;73:456–81.
[19] Bunger AP, Detournay E, Garagash DI. Toughness-dominated hydraulic fracture with leak-off. Int J Fract 2005;134:175–90.
[20] Garagash D, Detournay E. Plane-strain propagation of a fluid-driven fracture: small toughness solution. J Appl Mech 2005;72:916–28.
[21] Adachi J, Detournay E. Self-similar solution of a plane-strain fracture driven by a power-law fluid. Int J Numer Anal Meth Geomech 2002;26:579–604.
[22] Adachi J, Detournay E. Plane strain propagation of a hydraulic fracture in a permeable rock. Engng Fract Mech 2008;75:4666–94.
[23] Hu J, Garagash DI. Plane-strain propagation of a fluid-driven crack in a permeable rock with fracture toughness. ASCE J Engng Mech 2010;136(9):1152–66.
[24] Carter BJ et al. Simulating fully 3D hydraulic fracturing. In: Zaman M, Gioda G, Booker J, editors. Modeling in geomechanics. New York, NY: John Wiley & Sons; 2000.
[25] Devloo PRB et al. A finite element model for three dimensional hydraulic fracturing. Math Comput Simul 2006;73:142–55.
[26] Kresse O et al. Numerical modeling of hydraulic fractures interaction in complex naturally fractured formations. Rock Mech Rock Engng 2013;46:555–68.
[27] Ouyang S, Carey GF, Yew CH. An adaptive finite element scheme for hydraulic fracturing with proppant transport. Int J Numer Meth Fluids 1997;24(7):645–70.
[28] Siebrits E, Peirce AP. An efficient multi-layer planar 3D fracture growth algorithm using a fixed mesh approach. Int J Numer Meth Engng 2002;53:691–717.
[29] Vandamme L, Jeffrey RG, Curran JH. Pressure distribution in three-dimensional hydraulic fractures. SPE 15265 1988.
[30] Yamamoto K, Shimamoto T, Maezumi S. Development of a true 3D hydraulic fracturing simulator. SPE 54265 1999.
[31] Zhang X, Jeffrey RG, Thiercelin M. Mechanics of fluid-driven fracture growth in naturally fractured reservoirs with simple network geometries. J Geophys Res 2009;114:B12406.
[32] Sneddon IN, Lowengrub M. Crack problems in the classical theory of elasticity. New York: John Wiley & Sons; 1969.
[33] Chen ZR et al. Cohesive zone finite element-based modeling of hydraulic fracturing. Acta Mech Solida Sin 2009;22(5):443–52.
[34] Chen Z. Finite element modelling of viscosity-dominated hydraulic fractures. J Petrol Sci Engng 2012;88–89:136–44.
[35] Carrier B, Granet S. Numerical modeling of hydraulic fracture problem in permeable medium using cohesive zone model. Engng Fract Mech 2012;79:312–28.
[36] Papanastasiou P. An efficient algorithm for propagating fluid-driven fractures. Comput Mech 1999;24(4):258–67.
[37] Hunsweck MJ, Shen YX, Adrian JL. A finite element approach to the simulation of hydraulic fractures with lag. Int J Numer Anal Meth Geomech 2013;37(9):993–1015.
[38] Fu P, Johnson SM, Carrigan CR. An explicitly coupled hydro-geomechanical model for simulating hydraulic fracturing in arbitrary discrete fracture networks. Int J Numer Anal Meth Geomech 2012;37:2278–300.

[39] Gordeliy E, Detournay E. Implicit level set schemes for modeling hydraulic fractures using the XFEM. Comput Methods Appl Mech Engng 2013;266:125–43.
[40] Gordeliy E, Detournay E. Coupling schemes for modeling hydraulic fracture propagation using the XFEM. Comput Methods Appl Mech Engng 2013;253:305–22.
[41] Lecampion B. An extended finite element method for hydraulic fracture problems. Commun Numer Methods Engng 2009;25(2):121–33.
[42] Mohammadnejad T, Khoei AR. An extended finite element method for hydraulic fracture propagation in deformable porous media with the cohesive crack model. Finite Elem Anal Des 2013.
[43] Taleghani AD. Analysis of hydraulic fracture propagation in fractured reservoirs: an improved model for the interaction between induced and natural fractures. Austin: University of Texas; 2009.
[44] Batchelor GK. An introduction to fluid dynamics. Cambridge, UK: Cambridge University Press; 1967.
[45] Carter RD. Optimum fluid characteristics for fracture extension. In: Drilling and production practices. Tulsa: American Petroleum Institute; 1957.
[46] Boone TJ, Ingraffea AR. A numerical procedure for simulation of hydraulically-driven fracture propagation in poroelastic media. Int J Numer Anal Meth Geomech 1990;14(1):27–47.
[47] Guyan RJ. Reduction of stiffness and mass matrices. AIAA J 1965;3(2):380.
[48] Press WH et al. Numerical recipes in fortran: the art of scientific computing. New York: Cambridge University Press; 1992.
[49] Yau JF, Wang SS, Corten HT. A mixed-mode crack analysis of isotropic solids using conservation laws of elasticity. J Appl Mech 1980;47(2):335–41.
[50] Paris PC, Sih GC. In: A.S. 381, editor. Stress analysis of cracks, in fracture toughness testing and its application. American Society for Testing and Materials; 1965. p. 30–83.